



HAL
open science

Optical and Transport Properties of Metal–Oil Nanofluids for Thermal Solar Industry: Experimental Characterization, Performance Assessment, and Molecular Dynamics Insights

Iván Carrillo-Berdugo, Patrice Estellé, Elisa Sani, Luca Mercatelli, Ricardo Grau-Crespo, David Zorrilla, Javier Navas

► To cite this version:

Iván Carrillo-Berdugo, Patrice Estellé, Elisa Sani, Luca Mercatelli, Ricardo Grau-Crespo, et al.. Optical and Transport Properties of Metal–Oil Nanofluids for Thermal Solar Industry: Experimental Characterization, Performance Assessment, and Molecular Dynamics Insights. *ACS Sustainable Chemistry & Engineering*, 2021, 9 (11), pp.4194-4205. 10.1021/acssuschemeng.1c00053 . hal-03167612

HAL Id: hal-03167612

<https://hal.science/hal-03167612>

Submitted on 12 Mar 2021

HAL is a multi-disciplinary open access archive for the deposit and dissemination of scientific research documents, whether they are published or not. The documents may come from teaching and research institutions in France or abroad, or from public or private research centers.

L'archive ouverte pluridisciplinaire **HAL**, est destinée au dépôt et à la diffusion de documents scientifiques de niveau recherche, publiés ou non, émanant des établissements d'enseignement et de recherche français ou étrangers, des laboratoires publics ou privés.

Optical and transport properties of metal-oil nanofluids for thermal solar industry: experimental characterization, performance assessment and molecular dynamics insights

Iván Carrillo-Berdugo,^a Patrice Estellé,^b Elisa Sani,^c Luca Mercatelli,^c

Ricardo Grau-Crespo,^d David Zorrilla,^a Javier Navas^{a,*}

^a Departamento de Química Física, Facultad de Ciencias, Universidad de Cádiz, E-11510 Puerto Real (Cádiz), Spain

^b Univ Rennes, LGCGM, EA3913, F-35000, Rennes, France

^c CNR-INO National Institute of Optics, Largo E. Fermi, 6, I-50125 Firenze, Italy

^d Department of Chemistry, University of Reading, Whiteknights, Reading RG6 6DX, United Kingdom.

* Corresponding author: javier.navas@uca.es (J. Navas)

Abstract

Concentrating solar power (CSP) technology can become a very valuable contributor to the transformation and decarbonization of our energy landscape, but for this technology to overcome the barrier towards market deployment, significant enhancements in the solar-to-thermal-to-electric energy conversion efficiency are needed. Here, an in-depth experimental analysis of the optical and transport properties of Pd-containing aromatic oil-based nanofluids is presented, with promising results for their prospective use as volumetric absorbers and heat transfer fluids in next-generation parabolic-trough CSP plants. A 0.030 wt.% concentration of Pd nanoplates increases sunlight extinction by 90% after 20 mm propagation length and thermal conductivity by 23.5% at 373 K, which is enough to increase the overall system efficiency up to 45.3% and to reduce pumping requirements by 20%, with minimum increases in the collector length. In addition to that, molecular dynamics simulations are used to gain atomistic-level insights about the heat and momentum transfer in these nanofluids, with a focus on the role played by the solid-liquid interface in these phenomena. Molecules chemisorbed at the interface behave as a shelter-like boundary that hinders heat conduction, as a high thermal resistance path, and minimizes the impact of the solid on dynamic viscosity, as it weakens the interactions between the nanoplate and the surrounding non-adsorbed fluid molecules.

Keywords

Nanofluids; Concentrated Solar Power; Thermal performance; Molecular Dynamics; Sunlight extinction.

Introduction

Achieving sustainable development with secure, affordable and clean energy supply is a priority challenge for society. Fossil fuels remain the main energy source at global level: only 11% of the total final energy consumption in 2018 came from modern renewable energy technologies.¹ Concentrating solar power (CSP) has been recognized as a technology with the potential to make significant greenhouse gas emissions reductions and to provide power on demand through integrated thermal storage,^{2, 3} which consolidates reliable power blocks that can positively contribute for the penetration of solar energy in our energy consumption landscape and boost the decarbonization of our economies.

The limit in the operational value of CSP systems is the low solar-to-thermal-to-electric energy conversion efficiency; therefore, its improvement could accelerate the deployment of CSP technology. A promising strategy for such purpose is to use nanofluids^{4, 5} as heat transfer fluids (HTF). Nanofluids, compared to conventional HTF, exhibit enhanced thermophysical properties for convection heat transfer,⁶⁻¹² which is significant for heat transfer from the surface receiver to the HTF and from the HTF to the heat exchanger in the steam generator. Additionally, if their absorption and scattering properties provide enough optical efficiency^{10, 13-15}, some nanofluids can be used as volumetric absorbers in parabolic-trough receivers for directly harvesting concentrated solar radiation.¹⁶ Eggers et al.¹⁷ proved that the surface absorber requires very high Reynolds numbers to transfer the absorbed energy into the HTF and avoid overheating of the absorber tube. This demand of pumping power can be reduced significantly using volumetric absorption, as the temperature difference between the surface absorber and the fluid would be minimized and emissive losses consequently reduced.¹⁸

Here we report on the optical and transport properties of Pd-containing aromatic oil-based (Pd-AO) nanofluids for thermal solar industry with detailed experimental characterization results. The extinction coefficient in the UV-Vis-NIR range (300-2600 nm) and the sunlight extinction as a function of the path length are investigated, to verify if the presence of Pd nanoplates affects the spectral behaviour of the base fluid, potentially making these nanofluids good candidates for volumetric absorption. Thermal conductivity (as a function of the mass fraction of nanoplates and temperature) and dynamic viscosity (as a function of the shear rate, the mass fraction of nanoplates and temperature) are also studied, to assess thermal and flow requirements for the application. Based on these results and on density and specific heat characterizations from previous work,¹⁹ the overall efficiency of these nanofluids in both surface and volumetric parabolic-trough collectors (PTCs) and also in heat exchangers is assessed. We find that the characterized nanofluids, compared to their base fluid (the eutectic mixture of diphenyl oxide and biphenyl, commercially available as DowthermTM A), are superlative candidates for both volumetric absorption and heat transfer, as they exhibit full sunlight extinction at short path lengths and a notable increment in thermal conductivity, with negligible change in dynamic viscosity. The latter is an excellent yet very infrequently achieved condition, which may be related to the unique properties of the solid-liquid interface of these nanofluids. We provide insights on this issue by assessing the impact of the interfacial molecular layering on thermal conductivity and dynamic viscosity via classical molecular dynamics (MD) simulations. This phenomenon was already proven to exist and to play a key role on the anomalous enhancement in specific heat for these nanofluids,²⁰ but we demonstrate here that its effect goes beyond the impact on the specific heat.

Methodology

Nanofluid sample preparation – Nanofluids were prepared following a three-step formulation procedure: (i) Pd nanoplates were synthesized by mild chemical reduction of Pd^{2+} with polyvinyl pyrrolidone in a kinetically controlled solvothermal process;²¹ (ii) the host fluid was prepared by dilution of 1.0 wt.% of Triton X-100 surfactant in the base fluid Dowtherm™ A, given that mass fraction of Triton X-100 minimizes the dispersive surface tension component of the base fluid (and so does the solid-liquid interfacial tension) without a measurable change in its dynamic viscosity; (iii) Pd nanoplates (mainly triangular and hexagonal shaped with size distributions of 34.4 ± 10.0 nm and 78.2 ± 9.9 nm, respectively) in dry powder form were dispersed into the host fluid by ultrasonication. The colloid resulting from ultrasonication and its 1:2 and 1:5 dilutions, with mass fractions of 0.060 wt.%, 0.030 wt.% and 0.012 wt.% in Pd nanoplates, are the nanofluids whose thermal conductivity and dynamic viscosity are to be characterized. An in-depth description on the formulation procedure, together with the basic characterization of the nanomaterial and the stability of these nanofluid samples, is available elsewhere.¹⁹

Optical measurements – Spectral optical transmittance in the 300-2600 nm range of nanofluid samples and also of the base fluid and the host fluid (base fluid with 1.0 wt.% of Triton X-100 surfactant), for reference, was measured using a double-beam UV-VIS spectrophotometer (PerkinElmer Inc., LAMBDA 900), holding the sample in a variable-length cell.^{22, 23} Samples with mass fractions of 0.060 wt.%, 0.030 wt.% and 0.006 wt.% in Pd nanoplates are considered for characterization. A more diluted sample is required for the differences in sunlight extinction as a function of the mass fraction of nanomaterial to be better distinguished.

Thermal conductivity measurements – Thermal conductivity was measured using the non-destructive transient hot-bridge technique with a hot point sensor (THB-HPS) (Linseis GmbH, THB-100, sensor type C). The THB-HPS technique provides the highest possible accuracy in the transient measurement of thermal conductivity by minimising the error due to natural convection and keeps instrumental arrangement and sample preparation to a minimum. An input power of 32 mW was supplied to the source, which is sufficient for a good signal-to-noise ratio with negligible local convection during characterization of liquid samples. Measurement time was 10 s, with a delay of 30 s between measurements. Temperature was set at 298 K, 323 K, 348 K and 373 K by immersing cylindrical glass vials with 1.0 ml of liquid sample in individual jacketed vessels for homogeneous heating. Ten replicas were recorded for each sample and temperature, adding up to 200 data sets for post-processing and statistical analysis.

Rheological measurements – Steady-state shear flow behaviour and dynamic viscosity of the base fluid, the host fluid and all nanofluids were evaluated using a stress-controlled rheometer (Malvern Instruments Ltd, Kinexus PRO). The shear rate and viscosity data were collected applying a logarithmic shear stress ramp under steady-state condition to the samples loaded between a cone and plate geometry (60 mm cone diameter; 1° cone angle). Temperature of the samples is adjusted and controlled by a Peltier temperature control system with a precision of ± 0.1 K, below the upper plate. Also, both the sample and the cone and plate geometry are enclosed within thermal clovers. As for thermal conductivity, experiments were performed at 298 K, 323 K, 348 K and 373 K. At least two replicas were carried out for all samples without significant difference. Uncertainty in viscosity determination was evaluated comparing viscosity data of base fluid with manufacturer data. Additional information about the experimental procedure can be found in previous works.^{24, 25}

MD models – The structure and properties of solid-liquid interfaces have been proven to play a key role in energy and momentum transfer across them.²⁶⁻²⁸ Considering the enormous exposed surface of the disperse phase in nanofluids, the solid-liquid interface can be expected to significantly contribute to the nanofluid properties, and should therefore be studied in order to fully understand thermal and flow phenomena in these systems. Here we will consider three case scenarios for the solid-liquid interface of Pd-AO nanofluids, in which intermolecular interactions between species at these interfaces are defined attending to different physical chemistry backgrounds: (i) a physisorption-induced solid-liquid interface, in which no chemical interactions, beyond van der Waals effects, are allowed between the nanoparticle and the fluid molecules; (ii) an unhindered chemisorption-induced solid-liquid interface, in which both diphenyl oxide (DPO) and biphenyl (BP) can chemisorb on Pd surfaces; and (iii) a kinetically restricted chemisorption-induced solid-liquid interface, in which the activation energy requirement for DPO adsorption is considered so that only BP can chemisorb on Pd surfaces.

Optimised Potential for Liquid Simulation – All Atom (OPLS-AA) force field with parameters from LigParGen was considered for bonding and non-bonding interactions between atoms in the base fluid and a Morse potential with parameters by Yokoyama et al.²⁹ were also introduced to account for bonding interactions between Pd atoms in the nanostructure. Also, we parametrized a unique Morse potential from ab-initio calculations for the interaction between Pd atoms on the surface and C atoms of chemisorbed base fluid molecules in nanofluid models.²⁰ This is important, as the interfacial potential parameters were previously reported to be of great significance in order to correctly simulate heat transport in solid-liquid systems with the Green-Kubo method.²⁸ The Lorentz-Berthelot combining rules are used to parametrise the Lennard-Jones potential for pairwise interactions between odd atoms. Lennard-Jones pairwise interactions are limited to a cut-off distance of 10 Å. The particle-particle particle-mesh (PPPM) summation

method³⁰ was applied to compute long-range electrostatics. All atoms are explicitly included (no dummy atoms are used). A thorough description of the simulated systems (number of molecules, nanoplate aspect ratio, surface saturation) and the force field parametrization are available in Section I of the Supporting Information.

MD simulations – The Large Atomic/Molecular Massively Parallel Simulator (LAMMPS)^{31, 32} is the classical MD code of choice for the comprehensive study on the effect of the interfacial molecular layering on the transport properties of Pd-AO nanofluids. The initial configurations were created with Moltemplate,^{33, 34} a text-based molecular builder for LAMMPS. Periodic boundary conditions are imposed in all directions. The Verlet integration scheme³⁵ is used with a timestep of 1 fs. Velocities are rescaled with the Nosé-Hoover thermostat and barostat algorithms.³⁶⁻³⁹ The simulation run, with the above set-up, involves (i) a 10 ps run in NVE for relaxation, (ii) a 0.5 ns run in NVT for thermalization, (iii) a 1.5 ns run in NPT for equilibration, (iv) a 5 ns run in NVT for the computation of thermal conductivity and (v) a 5 ns run in NVT for the computation of dynamic viscosity. Both transport properties were computed using the Green-Kubo formalism^{40, 41}. Sampling interval (s) and correlation points (p) for flux data collection and correlation were selected for the above integrals to saturate in the calculation of transport properties with the base fluid model: $s = 5$ fs and $p = 1000$ were chosen for the calculation of thermal conductivity and $s = 5$ fs and $p = 10000$ were chosen for the calculation of dynamic viscosity. Dumping interval (d) is chosen to be $d = s \cdot p$ in all cases. The trajectories of the base fluid model and nanofluid models are all computed with this scheme at 298 K, 323 K, 348 K and 373 K and 1 atm (in line with experimental conditions), for a comparative analysis of the results on thermal conductivity and dynamic viscosity under different considerations for the interfacial molecular layering and, also, as a function of temperature.

Results and discussion

Optical characterization – The experimental spectral extinction coefficients are shown in Figure 1. It can be clearly seen that nanoplates modify the spectra of nanofluids with respect to the base fluid mainly in the UV-visible range, with monotonically decreasing curves extending towards the near infrared. For wavelengths longer than about 1600 nm, the contribution of nanoplates becomes negligible, and the spectrum of the base fluid is exactly reproduced.

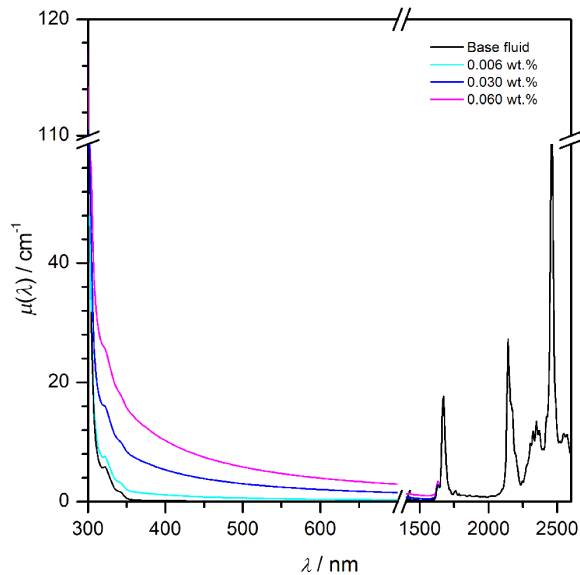


Figure 1. Spectral extinction coefficient of samples. The spectrum of the base fluid (black solid line) is also shown for reference.

The obtained spectral extinction coefficient $\mu(\lambda)$ allows us to give an estimation of the amount of sunlight attenuated during its propagation in the nanofluid volume. It can be expressed as a function of the propagation path length x , as follows^{42, 43}

$$\text{sunlight extinction } (x) = 1 - \frac{\int_{\lambda_{\min}}^{\lambda_{\max}} I(\lambda) \cdot e^{-\mu(\lambda)x} d\lambda}{\int_{\lambda_{\min}}^{\lambda_{\max}} I(\lambda) d\lambda} \quad (1)$$

where $I(\lambda)$ is the sunlight spectrum⁴⁴ and the integration is carried out in the whole range experimentally available ($\lambda_{\min} = 300$ nm, $\lambda_{\max} = 2600$ nm). Figure 2 compares the results for the nanofluids and base fluid.

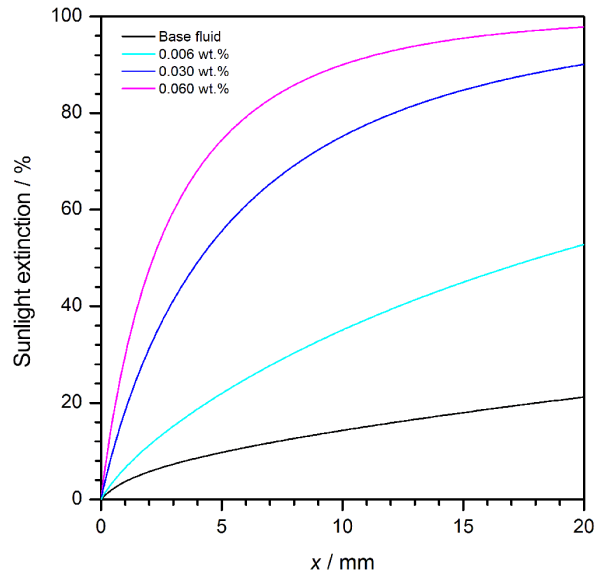


Figure 2. Sunlight extinction level as a function of the propagation path length within the liquid.

From Figure 2, we can see that, in the absence of nanoplates, the base fluid shows an attenuation of the incident sunlight of only 21% after 20 mm propagation path, resulting therefore not suitable for direct solar absorption. The addition of Pd nanoplates dramatically changes the interaction with solar radiation. In fact, even at the lowest investigated concentration, 0.006 wt.%, the sunlight attenuation in the nanofluid is more than doubled after a 20 mm path with respect to the base fluid (53% vs. 21%). At higher Pd nanoplate concentrations, sunlight attenuation

correspondingly increases, showing values of 75% and 90% after 10 mm and 90% and 98% after 20 mm for the samples with mass fractions of 0.030 wt.% and 0.060 wt.%, respectively.

The spatial distribution $S(x)$ of attenuated sunlight within the nanofluid can be calculated as well from the spectral extinction coefficient. It represents another important parameter to consider for assessing the samples potential for direct sunlight absorption. For the basic approximation of a cold fluid without convective mixing, which is a reasonable hypothesis if we aim to identify the optimized nanofluid composition for a given solar collector architecture and dimensioning and not to assess the actual temperature distribution in the nanofluid volume, it is expressed as:

$$S(x) = \frac{\int_{\lambda_{min}}^{\lambda_{MAX}} I(\lambda) \cdot \mu(\lambda) \cdot e^{\mu(\lambda)x} d\lambda}{\int_{\lambda_{min}}^{\lambda_{MAX}} I(\lambda) d\lambda} \quad (2)$$

The calculation is referred to the sunlight propagation from a single irradiated side, as it is the case of the radial direction in a PTC, or the thickness direction of a flat-plate collector. Figure 3 shows the plots for nanofluids and base fluid, according to Equation 2. For an easier readability, the curves are normalized to the highest value, obtained for the sample with the largest concentration at the input surface.

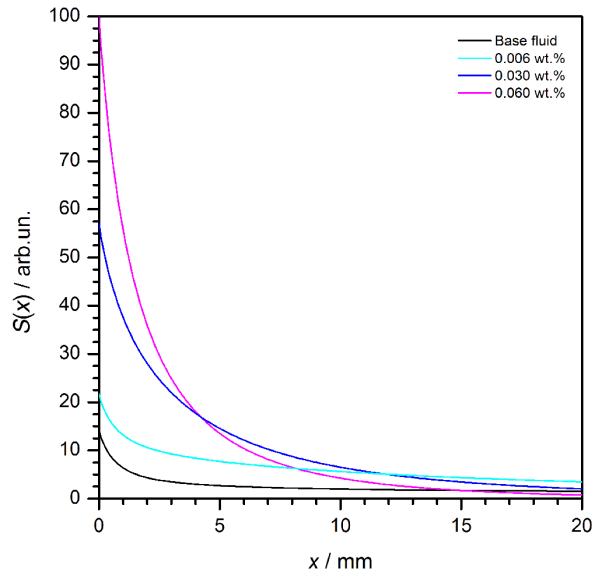


Figure 3. Spatial distributions of the energy locally stored in the fluids.

The undiluted nanofluid, that with the highest investigated concentration, is characterized by a distribution peaked near the input surface, with a strong gradient in the first 5 mm. Less concentrated samples result in a lower gradient and a deeper energy penetration in the liquid volume. The results in Figures 1, 2 and 3 constitute a tool for the colloid optimization, cross-referenced to the geometrical characteristics of the system where they have to be employed, although sufficient to conclude these nanofluids exhibit a suitable optical behaviour to be used as volumetric absorbers.

Thermal conductivity characterization – The transient hot-wire is, by far, the most used method for the measurement of thermal conductivity of nanofluids⁴⁵ because, compared to other methods, it reduces the impact of the natural convection in liquid samples on the measured signal and so errors in the derived thermal conductivities. The THB-HPS technique is a particular application of this method,⁴⁶ with an instrumental configuration to provide thermal and electrical self-

compensations. All thermal conductivity values here reported for Pd-AO nanofluid samples were acquired by means of the THB-HPS technique.

Conceptually, the hot-wire in a liquid sample is a line heat source immersed in an infinite isotropic material. The temperature rise, $\Delta T(r, t)$, at radial position r from the line source and time t , is given by

$$\Delta T(r, t) = \frac{q}{4\pi\kappa} \ln\left(\frac{4\alpha t}{r^2 e^\gamma}\right) \quad (3)$$

where q is the heat production per unit time and per unit length ($\text{W}\cdot\text{m}^{-1}$), κ is the thermal conductivity of the sample ($\text{W}\cdot\text{m}^{-1}\cdot\text{K}^{-1}$), α is the thermal diffusivity of the sample ($\text{m}^2\cdot\text{s}^{-1}$) and γ is the Euler-Mascheroni constant. The expression above can be linearized so that thermal conductivity κ can be determined from the slope of linear segments in $\Delta T(r, t)$ vs $\ln(t)$ datasets. In absence of convection, the ideal behaviour of $\Delta T(r, t)$ vs $\ln(t)$ curves is completely linear, but the existence of a local temperature difference inherently causes a local density difference that promotes natural convection. Such natural convection effect is equally present in the whole sample, if heated for characterization at higher temperatures. Thus, datasets acquired with the THB-HPS technique, for all samples and temperatures, were post-processed in order to choose the linear segment of the non-ideal measured signal for the derivation of thermal conductivity values. Figure 4A shows an instance of the shape of these curves and their linear segments for a particular replica from the characterization of the base fluid sample and a nanofluid sample at 373 K. Thermal conductivity values for each sample at all temperatures are presented in Figure 4B for discussion.

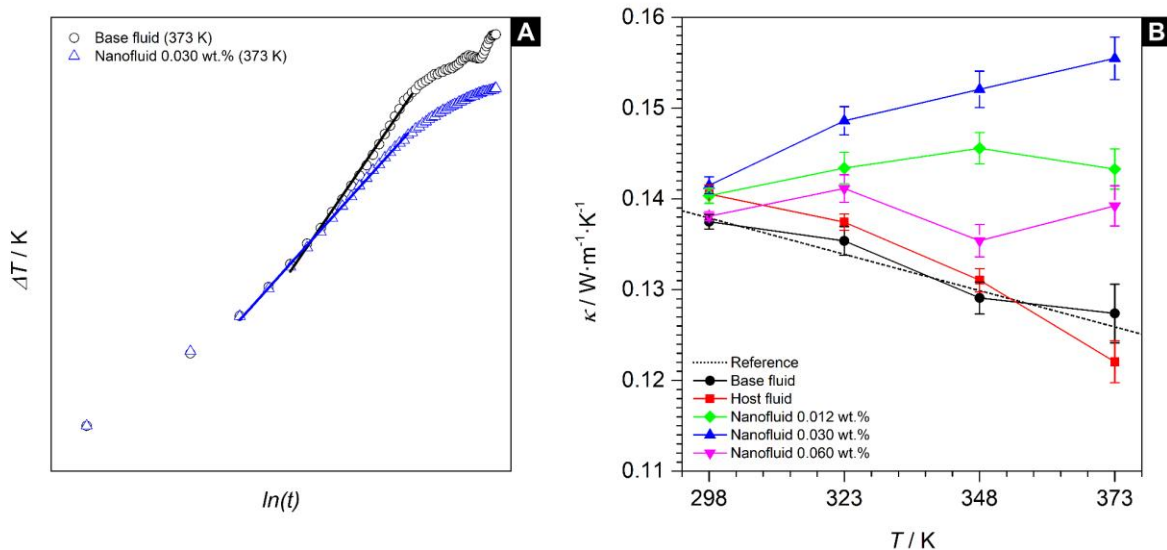


Figure 4. [A] Example of the acquired THB-HPS signals, represented by the temperature rise, as a function of the natural logarithm of time (only linear segments are considered for characterization purposes). [B] Thermal conductivity, as a function of temperature, for the base fluid, the host fluid and all nanofluid samples (solid lines do not represent data but are included as guide to the eye).

The thermal conductivity of the base fluid was measured in order to compare with commercially reported values. Our results match (by an average of 99.2%) the thermal conductivity values reported in the technical data sheet of DowthermTM A. The relative standard deviation at the highest temperature is 2.4%, which is consistent with the measurement uncertainties expected for the THB-100 (better than 2% for thermal conductivity according to the manufacturer). The above justifies the validity of the proposed experimental procedure. Thermal conductivity of the host fluid is also characterized, in order to verify if the addition of 1.0 wt.% Triton X-100 modifies the thermal conductivity of the base fluid. It seems to be the case at room temperature, but its significance vanishes at medium-high temperatures.

The thermal conductivity values of nanofluid samples are now examined. Maximum increments of 2.6%, 11.0%, 17.1% and 23.5% are found at 298 K, 323 K, 348 K and 373 K for the sample with a Pd content of 0.030 wt.%. It is remarkable that the sample with an intermediate mass fraction of Pd nanoplates exhibits the best enhancements in this transport property. The relative increments are almost halved for samples with Pd contents of 0.012 wt.% and 0.060 wt.%. Such a unique behaviour was also observed in a previous analysis of the specific heat of these nanofluid samples, which was also found to be maximized at intermediate mass fractions.¹⁹ A numerical model developed by Hentschke,⁴⁷ assuming the existence of interacting interfacial layers of fluid around nanoparticles, was found to successfully describe this behaviour of the specific heat. Yu and Choi created a numerical model⁴⁸ to calculate the effective thermal conductivity of a cubic arrangement of monodispersed spherical nanoparticles in a base fluid, in which solid-liquid interfaces exist and overlap. Compared to the Maxwell model,⁴⁹ the Hamilton-Crosser model⁵⁰ or their revised versions,^{51, 52} this cubic model provides a better description for this trend in thermal conductivity as a function of the mass fraction of nanomaterial. The effective thermal conductivity of the nanofluid increases up to a maximum from low to intermediate mass fractions, and then decreases for increasing mass fractions due to layer overlapping between adjacent particles. The discussion around it is conditioned by many parameters such as the interfacial layer thickness or the interfacial thermal conductivities, which are actually unknown and simply screened to assess their impact on the effective thermal conductivity. However, it is still relevant because it provides significance for the interfacial molecular layering and its role on the thermal conductivity of nanofluids. We previously proved such interfacial layer exists via DFT simulations¹⁹ and assessed how and how much it impacts the specific heat via MD simulations.²⁰ A similar analysis in terms of the transport properties is presented later in this paper.

Rheological characterization – The uncertainty of the experimental procedure for dynamic viscosity evaluation was first evaluated comparing experimental data with manufacturer data of Dowtherm™ A. As expected, and reported earlier,^{24, 25} the base fluid behaves in Newtonian manner in the shear rate range 10-1000 s⁻¹ for all tested temperatures, with a decrease of viscosity with temperature increase as shown in Figure 5A. An absolute average deviation of 3.8% in the range 298-373 K is obtained between experimental and manufacturer data demonstrating the goodness of experiments. Dynamic viscosity of the host fluids in the shear rate range 10-1000 s⁻¹ is also measured to evaluate in which way the presence of Triton X-100 can modify the dynamic viscosity of the base fluid. These results are presented in Figure 5B, evidencing the Newtonian behaviour of host fluids. In addition, a comparison of viscosity values between host and base fluids, reported in Figure 5A, shows an average absolute deviation of 2.8%. A slight increase in viscosity is noticed with the presence of the Triton X-100 but the value is within the experimental uncertainty domain. Finally, the shear flow behaviour and dynamic viscosity of nanofluids is reported in Figure 5B. The figure shows that the nanofluids also behave as Newtonian fluids with a really slight difference in viscosity value. Similar results were obtained at all temperatures. The slight difference between viscosity values of nanofluids and hosts fluids is also evidenced in Figure 5B. In the tested temperature range, the average increase in viscosity for the three concentrations in nanoparticles compared to host fluids is 1.4%, 2.3% and 3.8% (lower than experimental uncertainty) for mass fraction 0.012 wt.%, 0.030 wt.% and 0.060 wt.% respectively. Such a result is of significant relevance, as these nanofluids will not increase pumping power or pressure drop in CSP systems, compared to their base fluid.

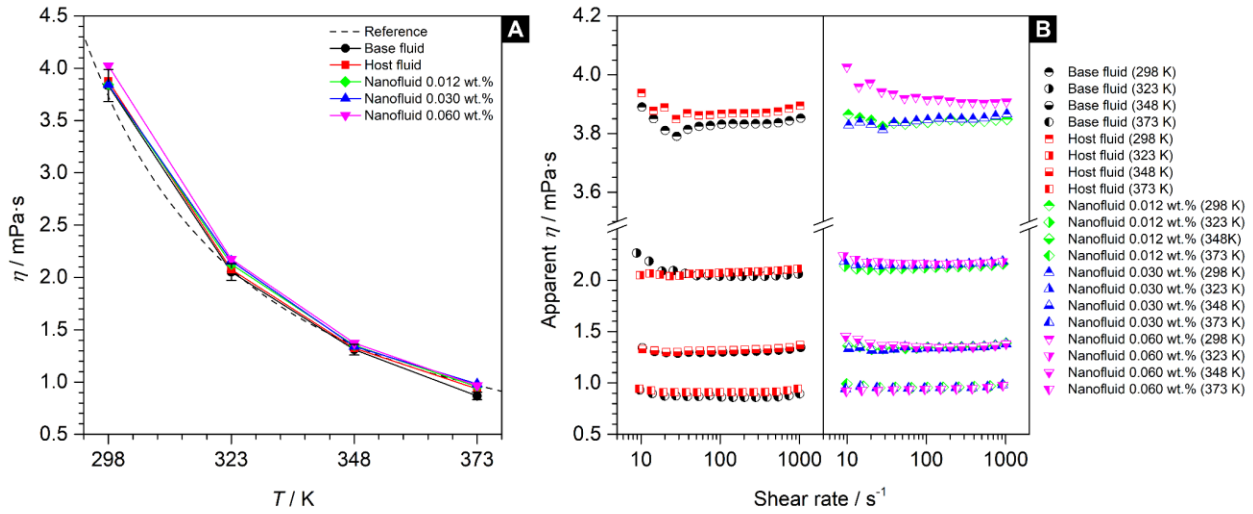


Figure 5. [A] Dynamic viscosity, as a function of temperature, for the base fluid, the host fluid and all nanofluid samples (solid lines do not represent data but are included as guide to the eye).

[B] Apparent viscosity values, as a function of the shear rate, for the same samples.

Assessment of solar collector efficiencies and heat exchangers effectiveness – The nanofluid samples we have examined are proven to provide the intended characteristics for volumetric absorption and heat transfer in the CSP sector. However, a complete assessment on the potential of these nanofluids for the application demands a realistic estimation of the dimensions and the expected thermal efficiency of surface and volumetric PTCs, which are one of the most mature CSP technologies in current use,⁵³ and also of the effectiveness of coupled heat exchangers, which are the primary units for steam generation.

We have calculated the expected outlet temperature of the HTF flowing through the PTC using two approximate analytic solutions developed by Bellos et al.⁵⁴ and O’Keeffe et al.⁵⁵ for steady state models of surface and volumetric PTCs under turbulent flow. We chose these models

because their authors kept simplifications and assumptions to a minimum and provided integrated expressions that include all possible parameters with influence on the system performance and can be solved directly with no computational cost. A more detailed revision on the explicit form of these expressions and parameters and their choice to be representative of an actual system is presented in Section II of the Supporting Information. Final results from these expressions are presented in Figure S1 and discussed here. We compare the outlet temperature, T_o , as a function of the total length of the array PTC modules, L , for different case scenarios with surface or volumetric absorbers, with DowthermTM A or the 0.030 wt.% Pd nanofluid sample (for which maximum enhancements in specific heat and thermal conductivity are found) as HTF, and different flow rates. The incident radiative heat flux, the width of the collector aperture, the efficiency of optical elements and pipe diameters are the same in all cases. The inlet temperature, $T_i = 473$ K, is also the same in all cases. The upper limit for the range of temperatures of interest is $T_{\max} = 673$ K, which is the maximum operating temperature for DowthermTM A stability not to be compromised. Our aims are to assess the required length of the PTC array and flow rate for each HTF to reach the maximum operating temperature ($T_o = T_{\max}$) in each type of collector, and determine which option is more cost-efficient.

The temperature rise per unit length is diminished for increasing flow rates under constant solar irradiation, but large flow rates are required so that turbulent regime is guaranteed for energy to be transferred from the surface to the HTF as it flows through the PTC in order to avoid local overheating¹⁷. This is particularly important in the case of surface PTC, not only for radiative losses to be minimized but also because surface overheating promotes thermal stress of the receiver and degradation of the absorbing coating, whose lifespan decays exponentially with temperature.⁵⁶ The flow rate, \tilde{v} , in a typical surface PTC is $\tilde{v} = 2.6 \text{ l}\cdot\text{s}^{-1}$ ($\text{Re} \approx 300000$). The

$T_o = T_{\max}$ condition for surface PTC, according to the results shown in Figure S1, is satisfied at $L \simeq 260$ m with DowthermTM A as HTF and $L \simeq 325$ m with the nanofluid sample as HTF.

A volumetric PTC with exactly the same geometry and flow rate than a surface PTC would meet the $T_o = T_{\max}$ condition at $L \simeq 340$ m with the nanofluid sample as HTF (volumetric absorption with DowthermTM A, as shown in Figure S1, is unfeasible from a practical perspective). In other words, a volumetric PTC with the same configuration than a surface PTC is less cost-efficient, because a larger PTC array would be required for the maximum operating temperature to be achieved. However, as the previously mentioned overheating problems do not apply for volumetric absorbers, flow rates can be significantly reduced. Particularly, given the storable energy density (i.e. the product of density and specific heat, $\rho \cdot c_P$) with the 0.030 wt.% Pd nanofluid sample is increased by 20% with respect to the base fluid (2443 $\text{kJ} \cdot \text{m}^{-3} \cdot \text{K}^{-1}$ for the nanofluid and 1943 $\text{kJ} \cdot \text{m}^{-3} \cdot \text{K}^{-1}$ for the base fluid),¹⁹ flow rates can be accordingly reduced by 20%, down to $\tilde{v} = 2.0 \text{ l} \cdot \text{s}^{-1}$ ($\text{Re} \simeq 240000$), so that the heat capacity rate is not modified. With this, the $T_o = T_{\max}$ condition for volumetric PTC is fulfilled at $L \simeq 270$ m. Do note that a longer PTC array is needed for those nanofluids whose specific heat is higher than that of the base fluid to be heated up to 673 K, but that does not necessarily imply that the performance of the system is lower. The thermal efficiency of the collector and the effectiveness of the coupled heat exchanger need to be assessed for an informed conclusion on the overall system performance to be drawn.

The thermal efficiencies, $\psi_{\text{collector}}$, associated to each solar collector can be calculated with the solutions derived by Bellos et al.⁵⁴ and O’Keeffe et al.⁵⁵ Alternatively, the number of transfer units (NTU) method has been considered for an estimation of the effectiveness, $\psi_{\text{exchanger}}$, of a heat exchanger in which phase change for one of the fluids (water evaporation) is assumed to

occur.⁵⁷ The overall system performance is given by $\psi_{\text{system}} = \psi_{\text{collector}} \cdot \psi_{\text{exchanger}}$. As for the previous calculations of outlet temperatures, full details are available in Section II of the Supporting Information and final results are presented here in Figure 6. Four sets are included in the diagram for data visualization: (i) surface PTC with the base fluid at $\tilde{v} = 2.6 \text{ l}\cdot\text{s}^{-1}$, (ii) surface PTC with the nanofluid sample at $\tilde{v} = 2.6 \text{ l}\cdot\text{s}^{-1}$, (iii) volumetric PTC with the base fluid at $\tilde{v} = 2.0 \text{ l}\cdot\text{s}^{-1}$, (iv) volumetric PTC with the nanofluid sample at $\tilde{v} = 2.0 \text{ l}\cdot\text{s}^{-1}$. Except for (iii), the other three configurations are found to provide similar collector thermal efficiencies, with variations below 1%. The effectiveness of the heat exchanger is found to be improved by 6% if the base fluid is replaced by the nanofluid sample as HTF, because the heat transfer rate per unit temperature, defined by the product of the overall heat transfer coefficient and the area, UA , is magnified as a consequence of the increased specific heat and thermal conductivity of the nanofluid compared to DowthermTM A (for a exchanger coil of 20 m, $UA_{(i)} = 3.7 \text{ kW}\cdot\text{K}^{-1}$, $UA_{(ii)} = 5.5 \text{ kW}\cdot\text{K}^{-1}$ and $UA_{(iv)} = 4.8 \text{ kW}\cdot\text{K}^{-1}$). The effectiveness of the heat exchanger is also increased by an additional 4% if the heat transfer nanofluid enters the exchanger with reduced flow rate, which occurs for volumetric PTCs, because the minimum heat capacity rate is reduced and that increases the NTU. The overall system maximum performance is found to be 45.3% for the volumetric PTC with the nanofluid sample as HTF with a flow rate of $2.0 \text{ l}\cdot\text{s}^{-1}$.

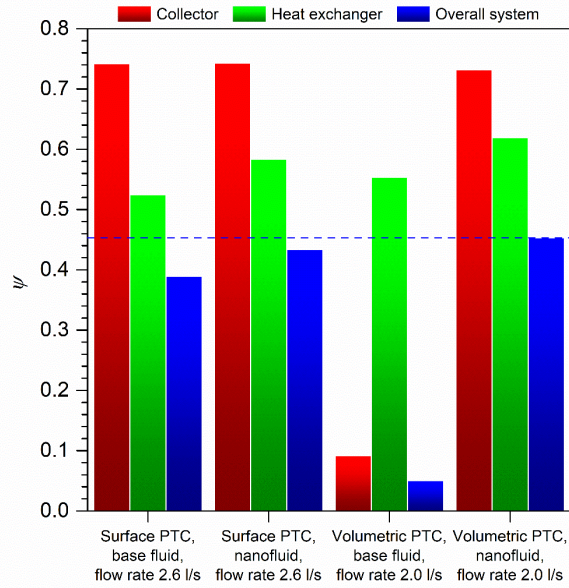


Figure 6. Expected collector thermal efficiency heat exchanger effectiveness and overall system performance for the different case scenarios under study (the dashed blue line indicates the maximum overall system performance).

To sum up, nanofluid-based volumetric PTCs, compared to the typical surface PTCs with DowthermTM A, do not suffer from overheating-induced thermal stresses and reduces the required amount of HTF and pumping requirements by 20%, with no limitations for the $T_o = T_{max} = 673$ K condition to be achieved but using a 4% longer PTC array only. Besides, the use of this nanofluid sample as HTF increases the global heat transfer coefficient in a heat exchanger for steam generation, as consequence of its improved thermophysical properties. The above analysis allowed us to conclude that the overall system peak performance increases up to 45.3% and that installation and maintenance costs, although tentatively, can be minimized (an actual assessment of the latter is out of the scope of this work). This is ultimately translated into more cost-efficient, optimized PTC-CSP plants.

Insights on transport properties from MD simulations – The goal of the theoretical part of this work is to assess how and how much the presence of an adsorbed molecular layer on the solid-liquid interface of nanofluids impacts their transport properties. To do so, we computed several MD trajectories with three nanofluid models representing different scenarios of interactions at the nanoparticle-fluid interface (those shown in Figure 7), for their response to changes in this state variable to be assessed as a function of temperature. Both transport properties were computed using the Green-Kubo formalism,^{40, 41} based on the integrals of time auto-correlation functions:

$$\kappa = \frac{V}{k_B T^2} \int_0^\infty \langle J(0) \cdot J(t) \rangle dt \quad (4)$$

$$\eta = \frac{V}{k_B T} \int_0^\infty \langle P(0) \cdot P(t) \rangle dt \quad (5)$$

where κ is the thermal conductivity, η is the dynamic viscosity, k_B is the Boltzmann constant, V is the equilibrium volume, T is the equilibrium temperature, $\langle J(0) \cdot J(t) \rangle$ is the heat flux vector auto-correlation function and $\langle P(0) \cdot P(t) \rangle$ is the auto-correlation function of the off-diagonal components of the stress tensor.

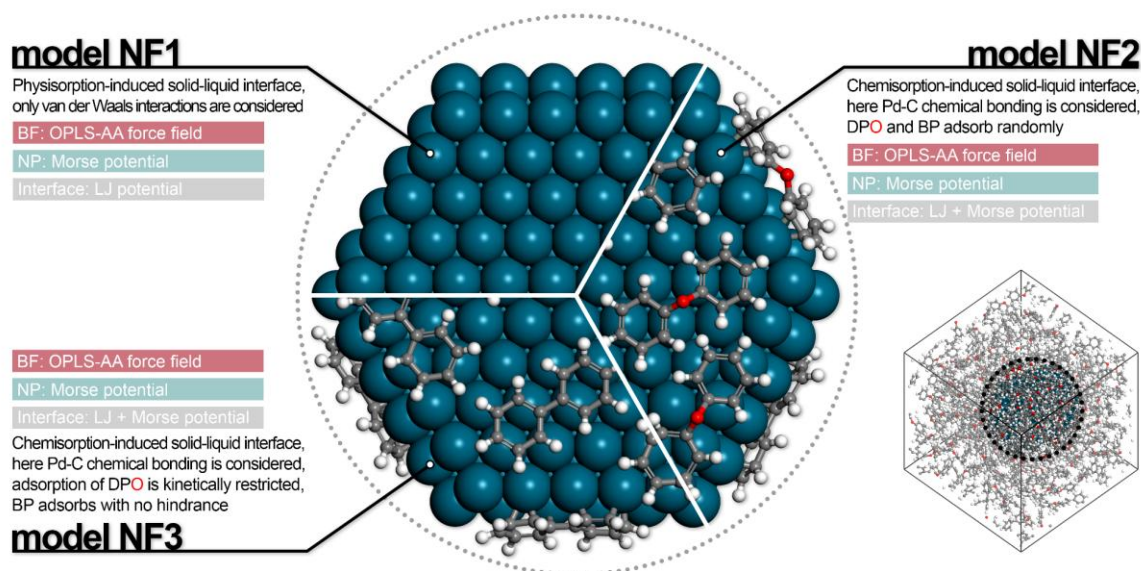


Figure 7. Summary of all MD models considered for this study. A description of each case scenario is given, together with the classical potential functions describing atomic interactions between atoms in the base fluid (BF), the nanoplate (NP) and the interface. A more detailed description is available in Section I of the Supporting Information.

Before using the simulation approach for understanding thermal and flow behaviour of these nanofluid systems, it is important to validate the force field parameters and the simulation set-up conditions by comparing computed results on thermal conductivity and dynamic viscosity for the base fluid, at 298 K, 323 K, 348 K and 373 K and 1 atm, with well-known experimental data available from the supplier. Computed data for transport properties of the base fluid model (filled black dots in Figure 8A and Figure 9A) are found to be in the same order of magnitude than experimental data (empty black dots in the same figures), albeit overestimated. The *compute heat/flux* command in LAMMPS has been recently reported^{58, 59} to produce anomalous values when the *compute stress/atom* command (which is necessary for the calculation of the per-atom

stress tensor in the heat flux) is applied to systems with many-body interactions (angles and dihedra), which is the case here. This might explain the overestimation of thermal conductivity values. The OPLS-AA force field has been previously reported to overestimate the Green-Kubo viscosity of organic liquids,⁶⁰ providing values two or three times larger than experimental observations. Still, both transport properties exhibited the expected response to changes in temperature. This is particularly significant because the decreasing thermal conductivity for increasing temperature is a very unique behaviour of this base fluid. The successful representation of the dynamics of the base fluid gives us confidence on the validity of the force field and simulation conditions.

In Figure 8A, the computed thermal conductivity values for nanofluid models are compared with each other and with the base fluid model. When it comes to comparisons with experimental results, the computed nanofluid thermal conductivities are clearly higher than expected, at all temperatures. This is not due to the technical (*compute* command) issues described above, which indistinctly appears in all nanofluid and base fluid models, but to the fact the mass of the Pd nanoplate with respect to the total mass of the simulation box is much higher, by two orders of magnitude, than the mass fractions contained in experimental samples. This is a limitation arising from the size of the simulation cell, which is necessarily restricted by computational cost. The discussion that follows is therefore qualitative and conceptual, not for quantitative prediction purposes.

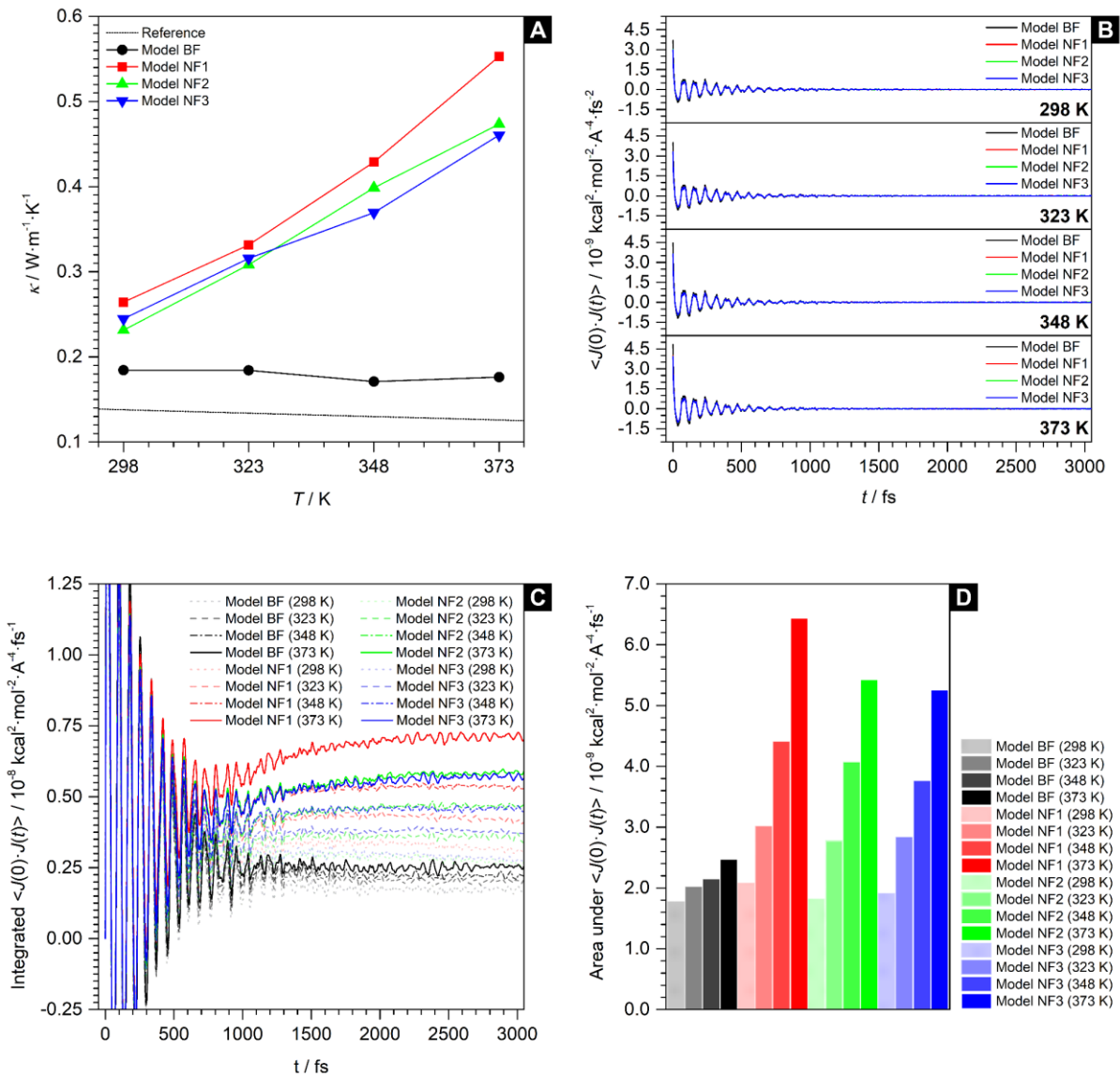


Figure 8. [A] Thermal conductivity values calculated from MD simulations with nanofluid and base fluid models, as a function of temperature (the solid lines do not represent data but are included as guide to the eye). [B] Time-averaged heat flux auto-correlation functions, $\langle J(0)\cdot J(t) \rangle$, for all models and temperatures (presented in LAMMPS *real* units). [C] Integrated $\langle J(0)\cdot J(t) \rangle$ functions. [D] Area under the $\langle J(0)\cdot J(t) \rangle$ functions.

The MD results reveal that thermal conductivity linearly increases for increasing temperatures in the nanofluids models, an opposite trend compared to the base fluid model, which is consistent with experimental results presented above. All nanofluid models here studied exhibit this behaviour with temperature, which indicates it must be mostly caused by the presence of the nanoplate, regardless of the nature of the solid-liquid interaction. The time-averaged heat flux auto-correlation functions, $\langle J(0) \cdot J(t) \rangle$, in Figure 8B, decays to zero and fluctuates around zero for all models under study, as expected for any system in true equilibrium. This means the chosen correlation time is long enough for the Green-Kubo method to provide consistent thermal conductivity values. However, it is quite difficult to highlight any differences between models by attending to these auto-correlation functions only, as the frequency and amplitude of the oscillatory fluctuations, and even the $J(0) \cdot J(0)$ value, are very similar in all cases. The integrated $\langle J(0) \cdot J(t) \rangle$ functions, in Figure 8C, reveal all models undergo a very similar decay pattern up to 0.5 ps, but the time for correlation loss (i.e. the required time for the integral of $\langle J(0) \cdot J(t) \rangle$ to saturate) is ~ 1.5 ps for the base fluid model at all temperatures and ~ 1.5 ps, ~ 1.7 ps, ~ 2.2 ps and ~ 2.5 ps for nanofluid models at 298 K, 323 K, 348 K and 373 K, respectively. The values from the cumulative integration up to this point, independently reported in Figure 8D, are also found to increase with temperature in all cases and to be larger for all nanofluid models compared to the base fluid model. The fluctuations around the saturation point are sufficiently small for these values to be unequivocally distinguished from each other. Besides, the $J(t)$ vector includes a V^{-1} scaling factor, meaning the values reported in Figure 8D are intensive, so that any differences between them are independent of the number of atoms in the system and only dependent of its dynamics. The information obtained from $\langle J(0) \cdot J(t) \rangle$ functions and their integrated counterparts allows us to conclude that thermal conductivity enhancements in these nanofluids models can be

due to an increase in the mean free path of thermal vibrations, because it takes longer for heat to dissipate according to the correlation loss times. Also, minimum changes are observed in the decay pattern of $\langle J(0) \cdot J(t) \rangle$ with respect to the base fluid, suggesting the nanoplate has a local influence on the nanofluid enhanced heat conduction, which involves the solid phase and the interface but does not affect the base fluid any further.

Thermal transport across the solid-liquid interface is sensitive to the mode of adsorption of those molecules. According to the results in Figure 8A, models NF2 and NF3, with chemisorption-induced solid-liquid interfaces in which base fluid molecules are bonded to the surface, show thermal conductivity values lower by an average 10.5% compared to model NF1, with a physisorption-induced solid-liquid interface in which no interactions between base fluid molecules and the surface beyond van der Waals forces exist. The integrated areas are, indeed, smaller for models NF2 and NF3 than for model NF1, which means heat transfer is significantly worsen for the chemisorption-induced interface models compared to the physisorption-induced one. That difference becomes even more strongly marked as temperature increases. Base fluid molecules in this chemisorption-induced interfacial layer molecules directly distort the atomic-level structure of the nanoplate surface, interrupting the propagation of thermal vibrations. Interfacial layering is a shelter-like boundary of high thermal resistance that hinders heat conduction. Given the thermal conductivity for models NF2 and NF3 is lower than for model NF1, the interfacial thermal resistance in models NF2 and NF3 is expected to be larger than in model NF1. This effect does not seem to depend on the nature of chemisorbed species, as it can be appreciated by comparing thermal conductivities of model NF2 (chemisorbed DPO and BP) and model NF3 (chemisorbed BP only).

We also investigated if a dependency of heat conduction with the directions of the system exists by analysing the spatial components of $\langle J(0) \cdot J(t) \rangle$ functions, that is $\langle J_x(0) \cdot J_x(t) \rangle$, $\langle J_y(0) \cdot J_y(t) \rangle$ and $\langle J_z(0) \cdot J_z(t) \rangle$. These components were found to be undistinguishable from each other. We verified the nanoplate does not rotate during the simulation, so this isotropic heat conduction is not a consequence of time average over different orientations. Although the 2D morphology of the nanomaterials is likely to exhibit anisotropic heat conduction, the aspect ratio of the nanostructure may not be sufficient for anisotropy to appear.

We now focus on the computed dynamic viscosity values, plotted in Figure 9A. Here, as for thermal conductivity, the discussion around MD results is qualitative and not intended for prediction purposes when compared to experimental results, due to the limitations imposed by the enormous mass fraction of Pd in the simulation box. All nanofluid models as well as the base fluid model exhibit an exponentially decreasing viscosity for increasing temperatures, in clear parallelism with experimental results. The auto-correlation functions of the off-diagonal components of the stress tensor, $\langle P(0) \cdot P(t) \rangle$, in Figure 9B, decay to zero within the timeframe provided by the chosen correlation time. Given this condition, the Green Kubo method is also expected to provide reliable viscosity values. Unfortunately, as for the $\langle J(0) \cdot J(t) \rangle$ functions, it is difficult to set the parameters for a discussion around the $\langle P(0) \cdot P(t) \rangle$ functions, since the differences in oscillatory decay pattern, between systems at a given temperature, are minimal. For that, we go to their integrated counterparts, presented in Figure 9C, in which is evident that much longer times are required for the Green-Kubo integral to saturate, meaning the time for correlation loss in the $\langle P(0) \cdot P(t) \rangle$ functions is consequently longer. The dissipation of shear stress (or momentum flux) to equilibrium is, compared to the dissipation of heat flux, a slower process by one order of magnitude. Times for correlation loss are ~ 100 ps, ~ 90 ps, ~ 70 ps and ~ 60 ps at

298 K, 323 K, 348 K and 373 K, respectively, with no significant differences between models. It was not possible to accurately establish the time for correlation loss for the models at 298 K, as the plateau region is not as well defined as for the rest of temperature. The upper limit of correlation time was chosen in these cases, as a fair approximation for comparison purposes within an accessible simulation time scale. The values from the cumulative integration up to this point, in Figure 9D, are also found to decrease with temperature in all cases. It all explains why dynamic viscosity values from all models converge at the highest temperature.

The shear stress, as the heat flux, is also sensitive to the mode of adsorption. Models NF2 and NF3, with chemisorption-induced solid-liquid interfaces, show dynamic viscosity values lower by 9.4% at 298 K compared to model NF1, with a physisorption-induced solid-liquid interface. Although times for correlation loss are very similar, the integrated areas are, in fact, smaller for models NF2 and NF3. This means the internal frictional force that arises between the nanoplate and the adjacent base fluid molecules in perpetual motion during the MD trajectories is significantly smaller in models NF2 and NF3 than in model NF1, as the interactions between the nanoplate and the surrounding fluid molecules are weaker for being mediated by those molecules permanently chemisorbed at the interface. Here again, the nature of the chemisorbed species is not really significant, as it can be appreciated by comparing dynamic viscosities of model NF2 (DPO and BP) and model NF3 (BP only). As for heat transfer, no dependency on momentum transfer with the directions of the system was found by analysing the individual auto-correlation function for each component of the stress tensor, $\langle P_{xy}(0) \cdot P_{xy}(t) \rangle$, $\langle P_{xz}(0) \cdot P_{xz}(t) \rangle$ and $\langle P_{yz}(0) \cdot P_{yz}(t) \rangle$.

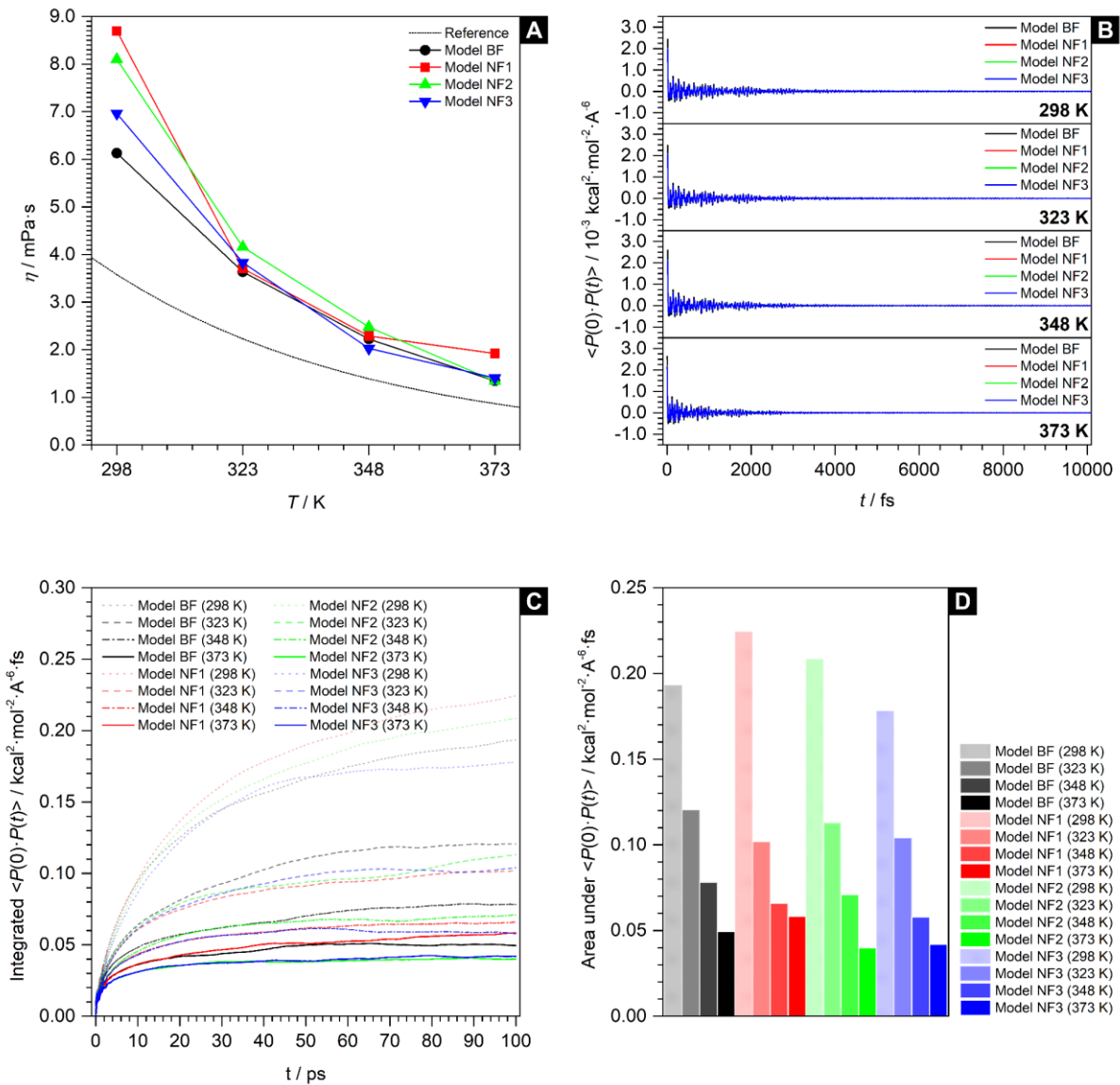


Figure 9. [A] Dynamic viscosity values calculated from MD simulations with nanofluid and base fluid models, as a function of temperature (the solid lines do not represent data but are included as guide to the eye). [B] Time-averaged auto-correlation functions of the off-diagonal components of the stress tensor, $\langle P(0) \cdot P(t) \rangle$, for all models and temperatures (presented in LAMMPS *real* units). [C] Integrated $\langle P(0) \cdot P(t) \rangle$ functions. [D] Area under the $\langle P(0) \cdot P(t) \rangle$ functions.

Conclusions

We have presented a detailed analysis on the potential of aromatic oil-based nanofluids with Pd nanoplates as a volumetric absorbers and heat transfer fluids for concentrated solar power systems, with experimental results on optical and transport properties revealing these nanofluids are promising candidates for the application. The sunlight extinction level hits 53%, 90% and 98% after a propagation length of 20 mm for mass fractions of 0.006 wt.%, 0.030 wt.% and 0.060 wt.%, which is a good indicator for these nanofluids to be used as volumetric absorbers. Thermal conductivity is found to be increased by 2.6%, 11.0%, 17.1% and 23.5% at 298 K, 323 K, 348 K and 373 K for an intermediate mass fraction of 0.030 wt.%. Dynamic viscosity, in the range of concentrations and temperatures under study, remains unchanged, as no measured differences could be distinguished from experimental uncertainty. Results from characterization allowed us to carry out a realistic assessment of the outlet temperature profiles in surface and volumetric parabolic-trough collectors using these nanofluids. It was concluded that, compared to the typical surface parabolic-trough collector with DowthermTM A, volumetric absorption with these nanofluid samples increases the overall system efficiency up to 45.3% and reduces pumping requirements by 20%, with minimum increases in the collector length, thus becoming more cost-efficient than current technology. Molecular dynamics revealed the impact of the nanoplate on the overall nanofluid heat transfer and momentum transfer, which are respectively quantified by thermal conductivity and dynamic viscosity, are limited to a local scale and sensitive to the mode of adsorption of base fluid molecules on the solid-liquid interface. This finding suggests that engineering interactions at the solid-liquid interface could become an innovative approach to further improve the thermophysical properties of nanofluids, and encourages the discussion on what solid-liquid pairs are of potential interest and should therefore

be tested as candidates for volumetric absorption and heat transfer in concentrating solar power systems.

Supporting Information

Supporting information includes (i) description of models and classical potentials for molecular dynamics simulations and (ii) expressions and parameters for the calculation of outlet temperatures and efficiencies of parabolic-trough collectors and the effectiveness of heat exchangers.

Author contributions

I.C.-B. contributed to thermal conductivity measurements, molecular dynamics simulations, revision and discussion of results and writing of the paper; P.E. contributed to rheological measurements, discussion of results and writing of the paper; E.S. and L.M. contributed to optical measurements, discussion of results and writing of the paper; R.G.-C. contributed to molecular dynamics simulations, discussion of results and writing of the paper; D.Z. contributed to molecular dynamics simulations and discussion of results; J.N. contributed to the direction of the work, revision and discussion of results and writing of the paper.

Conflicts of Interest

The authors declare no competing financial interests.

Acknowledgments

I.C.-B. acknowledges FPU16/02425 studentship from *Ministerio de Universidades del Gobierno de España*. J.N. acknowledges *Ministerio de Ciencia e Innovación del Gobierno de España* for funding under Grant No. RTI2018-096393-B-I00 and for financial support related to the measurement of thermal properties with devices acquired under Grant No. UNCA15-CE-2945. This work made use of CAI3, the high-performance computing service at *Universidad de Cádiz*.

References

1. REN21 *Renewables 2019 Global Status Report*; REN21: Paris, France, 2020.
2. Lovegrove, K.; Stein, W., *Concentrating Solar Power Technology: Principles, Developments and Applications*. 1st ed.; Woodhead Publishing: United Kingdom, 2012.
3. Forrester, J., The Value of CSP with Thermal Energy Storage in Providing Grid Stability. *Energy Procedia* **2014**, *49*, 1632-1641.
4. Masuda, H.; Ebata, A.; Teramae, K.; Hishinuma, N., Alteration of Thermal Conductivity and Viscosity of Liquid by Dispersing Ultra-fine Particles (Dispersion of γ -Al₂O₃, SiO₂, and TiO₂ Ultra-fine Particles). *Netsu Bussei* **1993**, *7*, 227-233.
5. Choi, S. U. S.; Eastman, J. A., Enhancing Thermal Conductivity of Fluids with Nanoparticles. In *ASME IMECE*, 1995; Vol. 231, pp 99-106.
6. Manikandan, S.; Rajan, K. S., MgO-Therminol 55 Nanofluids for Efficient Energy Management: Analysis of Transient Heat Transfer Performance. *Energy* **2015**, *88*, 408-416.
7. Colangelo, G.; Favale, E.; Miglietta, P.; Milanese, M.; De Risi, A., Thermal Conductivity, Viscosity and Stability of Al₂O₃-Diathermic Oil Nanofluids for Solar Energy Systems. *Energy* **2016**, *95*, 124-136.
8. Gómez-Villarejo, R.; Martín, E. I.; Navas, J.; Sánchez-Coronilla, A.; Aguilar, T.; Gallardo, J. J.; Alcántara, R.; De los Santos, D.; Carrillo-Berdugo, I.; Fernández-Lorenzo, C., Ag-based Nanofluidic System to Enhance Heat Transfer Fluids for Concentrating Solar Power: Nano-level Insights. *Appl. Energy* **2017**, *194*, 19-29.
9. Teruel, M.; Aguilar, T.; Martínez-Merino, P.; Carrillo-Berdugo, I.; Gallardo, J. J.; Gómez-Villarejo, R.; Alcántara, R.; Fernández-Lorenzo, C.; Navas, J., 2D MoSe₂-based

nanofluids prepared by liquid phase exfoliation for heat transfer applications in concentrating solar power. *Sol. Energ. Mat. Sol. C.* **2019**, *200*, 109972, 1-11.

10. Aguilar, T.; Sani, E.; Mercatelli, L.; Carrillo-Berdugo, I.; Torres, E.; Navas, J., Exfoliated Graphene Oxide-based Nanofluids with Enhanced Thermal and Optical Properties for Solar Collectors in Concentrating Solar Power. *J. Mol. Liq.* **2020**, *306*, 112862, 1-9.

11. Chen, Y. Y.; Walvekar, R.; Khalid, M.; Shahbaz, K.; Gupta, T. C. S. M., Stability and Thermophysical Studies on Deep Eutectic Solvent-based Carbon Nanotube Nanofluid. *Mater. Res. Express* **2017**, *4*, 075028, 1-16.

12. Ilyas, S. U.; Pendyala, R.; Narahari, M., Stability and Thermal Analysis of MWCNT – Thermal Oil-based Nanofluids. *Colloids Surf., A* **2017**, *527*, 11-22.

13. Hordy, N.; Rabilloud, D.; Meunier, J.-L.; Coulombe, S., High Temperature and Long-term Stability of Carbon Nanotube Nanofluids for Direct Absorption Solar Thermal Collectors. *Solar Energy* **2014**, *105*, 82-90.

14. Gimeno-Furio, A.; Hernandez, L.; Navarrete, N.; Mondragon, R., Characterisation Study of a Thermal Oil-based Carbon Black Solar Nanofluid. *Renew. Energ.* **2019**, *140*, 493-500.

15. Lee, R.; Kim, J. B.; Qin, C.; Lee, H.; Lee, B. J.; Jung, G. Y., Synthesis of Therminol-based Plasmonic Nanofluids with Core/Shell Nanoparticles and Characterization of their Absorption/Scattering Coefficients. *Sol. Energy Mater. Sol. Cells* **2020**, *209*, 110442, 1-8.

16. Khullar, V.; Tyagi, H.; Phelan, P. E.; Otanicar, T. P.; Singh, H.; Taylor, R. A., Solar Energy Harvesting Using Nanofluids-Based Concentrating Solar Collector. *J. Nanotechnol. Eng. Med.* **2012**, *3*, 031003, 1-9.

17. Eggers, J. R.; Lange, E. M.; Kabelac, S., Radiation and Energetic Analysis of Nanofluid Based Volumetric Absorbers for Concentrated Solar Power. *Nanomaterials* **2018**, *8*, 838, 1-24.

18. Lenert, A.; Wang, E. N., Optimization of Nanofluid Volumetric Receivers for Solar Thermal Energy Conversion. *Sol. Energy* **2012**, *86*, 253-265.
19. Carrillo-Berdugo, I.; Midgley, S.; Zorrilla, D.; Grau-Crespo, R.; Navas, J., Understanding the Specific Heat Enhancement in Metal-containing Nanofluids for Thermal Energy Storage: Experimental and Ab-initio evidence for a Strong Interfacial Layering Effect. *ACS Appl. Energy Mater.* **2020**, *3*, 9246–9256.
20. Carrillo-Berdugo, I.; Grau-Crespo, R.; Zorrilla, D.; Navas, J., Interfacial molecular layering enhances specific heat of nanofluids: evidence from molecular dynamics. *J. Mol. Liq.* **2020**, *325*, 115217, 1-8.
21. Lim, B.; Jiang, M.; Tao, J.; Camargo, P. H. C.; Zhu, Y.; Xia, Y., Shape-Controlled Synthesis of Pd Nanocrystals in Aqueous Solutions. *Adv. Funct. Mater.* **2009**, *19*, 189-200.
22. Sani, E.; Dell'Oro, A., Optical constants of ethylene glycol over an extremely wide spectral range. *Opt. Mater.* **2014**, *37*, 36-41.
23. Sani, E.; Dell'Oro, A., Spectral optical constants of ethanol and isopropanol from ultraviolet to far infrared. *Opt. Mater.* **2016**, *60*, 137-141.
24. Gómez-Villarejo, R.; Estellé, P.; Navas, J., Boron nitride nanotubes-based nanofluids with enhanced thermal properties for use as heat transfer fluids in solar thermal applications. *Sol. Energ. Mat. Sol. C.* **2020**, *205*, 110266, 1-13.
25. Martínez-Merino, P.; Midgley, S.; Martín, E. I.; Estellé, P.; Alcántara, R.; Sánchez-Coronilla, A.; Grau-Crespo, R.; Navas, J., Novel WS₂-Based Nanofluids for Concentrating Solar Power: Performance Characterization and Molecular-Level Insights. *ACS Appl. Mater. Interfaces* **2020**, *12*, 5793-5804.

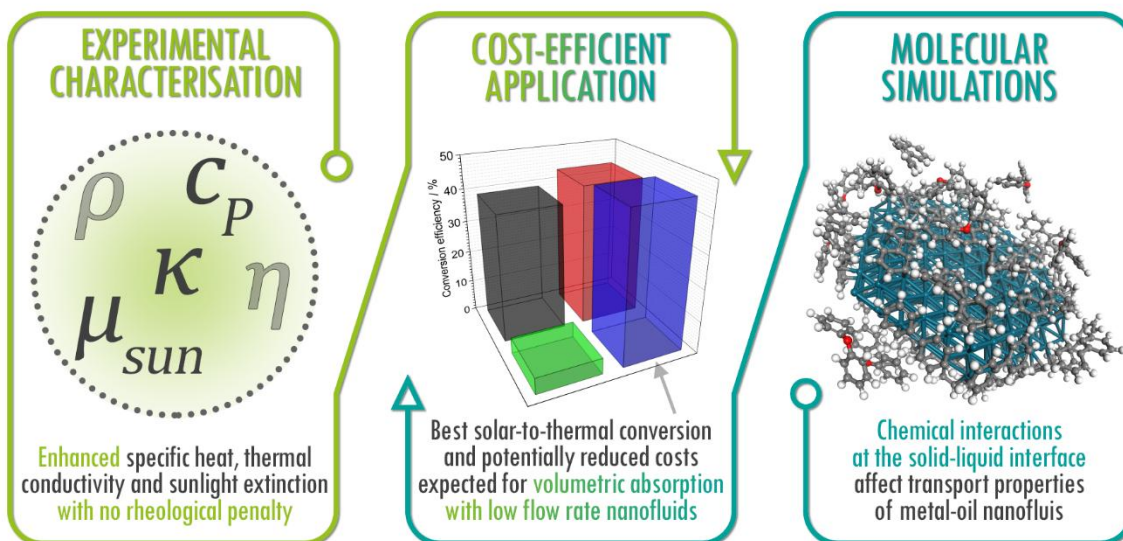
26. Torii, D.; Ohara, T.; Ishida, K., Molecular-Scale Mechanism of Thermal Resistance at the Solid-Liquid Interfaces: Influence of Interaction Parameters Between Solid and Liquid Molecules. *J. Heat Transfer*. **2010**, *132*, 012402, 1-9.
27. Wei, X.; Zhang, T.; Luo, T., Thermal Energy Transport across Hard–Soft Interfaces. *ACS Energy Lett.* **2017**, *2*, 2283-2292.
28. Akiner, T.; Kocer, E.; Mason, J. K.; Ertuck, H., Green–Kubo assessments of thermal transport in nanocolloids based on interfacial effects. *Mater. Today Commun.* **2019**, *20*, 100533, 1-6.
29. Yokoyama, T.; Ohta, T., Temperature-Dependent EXAFS Study on Supported Silver and Palladium Clusters: Comparison on Their Interatomic Potentials with Those of Bulk Metals. *Jpn. J. Appl. Phys.* **1990**, *29*, 2052-2058.
30. Hockney, R. W.; Eastwood, J. W., *Computer Simulation Using Particles*. 1st ed.; Taylor & Francis Group: Abingdon, UK, 1988.
31. Plimpton, S.; Thompson, A.; Moore, S.; Kohlmeyer, A.; Berger, R. *Large Atomic/Molecular Massively Parallel Simulator (LAMMPS)*, 17Nov2016; 2016.
32. Plimpton, S., Fast Parallel Algorithms for Short-Range Molecular Dynamics. *J. Comput. Phys.* **1995**, *117*, 1-19.
33. Jewett, A. *Moltemplate*, 1.34; 2015.
34. Jewett, A. I.; Zhuang, Z.; Shea, J.-E., Moltemplate a Coarse-Grained Model Assembly Tool. *Biophys. J.* **2013**, *104*, 169a.
35. Verlet, L., Computer "Experiments" on Classical Fluids. I. Thermodynamical Properties of Lennard-Jones Molecules. *Phys. Rev. A* **1967**, *159*, 98-103.
36. Nosé, S., A Molecular Dynamics Method for Simulations in the Canonical Ensemble. *Mol. Phys.* **1984**, *52*, 255-268.

37. Nosé, S., A Unified Formulation of the Constant Temperature Molecular Dynamics Methods. *J. Chem. Phys.* **1984**, *81*, 511-519.
38. Hoover, W. G., Canonical Dynamics: Equilibrium Phase-space Distributions. *Phys. Rev. A* **1985**, *1985*, 1695-1697.
39. Hoover, W. G., Constant-Pressure Equations of Motion. *Phys. Rev. A* **1986**, *34*, 2499-2500.
40. Green, M. S., Markoff Random Processes and the Statistical Mechanics of Time-Dependent Phenomena. II. Irreversible Processes in Fluids. *J. Chem. Phys.* **1954**, *22*, 398-413.
41. Kubo, R., Statistical-Mechanical Theory of Irreversible Processes. I. General Theory and Simple Applications to Magnetic and Conduction Problems. *J. Phys. Soc. Jpn.* **1957**, *12*, 570-586.
42. Sani, E.; Barison, S.; Pagura, C.; Mercatelli, L.; Sansoni, P.; Fontani, F.; Jafrancesco, D.; Francini, F., Carbon Nanohorns-based Nanofluids as Direct Sunlight Absorbers. *Opt. Express* **2010**, *18*, 5179-5187.
43. Sani, E.; Mercatelli, L.; Barison, S.; Pagura, C.; Agresti, F.; Colla, L.; Sansoni, P., Potential of carbon nanohorn-based suspensions for solar thermal collectors. *Sol. Energ. Mat. Sol. C* **2011**, *95*, 2994-3000.
44. ASTM, Standard Tables for Reference Solar Spectral Irradiances: Direct Normal and Hemispherical on 37° Tilted Surface. 2012; Vol. G173-03.
45. Paul, G.; Chopkar, M.; Manna, I.; Das, P. K., Techniques for measuring the thermal conductivity of nanofluids: A review. *Renew. Sust. Energ. Rev.* **2010**, *14*, 1913-1924.
46. Hammerschmidt, U.; Meier, V., New Transient Hot-Bridge Sensor to Measure Thermal Conductivity, Thermal Diffusivity, and Volumetric Specific Heat. *Int. J. Thermophys.* **2006**, *27*, 840-864.

47. Hentschke, R., On the Specific Heat Capacity Enhancement in Nanofluids. *Nanoscale Res. Lett.* **2016**, *11*, 88, 1-11.
48. Yu, W.; Choi, S. U. S., An Effective Thermal Conductivity Model of Nanofluids with a Cubical Arrangement of Spherical Particles. *J. Nanosci. Nanotechnol.* **2005**, *5*, 580-586.
49. Maxwell, J. C., *A Treatise on Electricity and Magnetism, Vol. I.* 1st ed.; Clarendon Press: Oxford, UK, 1873.
50. Hamilton, R. L.; Crosser, O. K., Thermal Conductivity of Heterogeneous Two-component Systems. *Ind. Eng. Chem. Fundamentals* **1962**, *1*, 187-191.
51. Yu, W.; Choi, S. U. S., The role of interfacial layers in the enhanced thermal conductivity of nanofluids: A renovated Maxwell model. *J. Nanopart. Res.* **2003**, *5*, 167-171.
52. Yu, W.; Choi, S. U. S., The role of interfacial layers in the enhanced thermal conductivity of nanofluids: A renovated Hamilton–Crosser model. *J. Nanopart. Res.* **2004**, *6*, 355-361.
53. Kalogirou, S. A., Solar thermal collectors and applications. *Prog. Energy Combust. Sci.* **2004**, *30*, 231-295.
54. Bellos, E.; Tzivanidis, C., Analytical Expression of Parabolic Trough Solar Collector Performance. *Designs* **2018**, *2*, 9, 1-17.
55. O'Keeffe, G. J.; Mitchell, S. L.; Myers, T. G.; Cregan, V., Modelling the Efficiency of a Nanofluid-based Direct Absorption Parabolic Trough Solar Collector. *Sol. Energy* **2018**, *159*, 44-54.
56. Raccurt, O.; Matino, F.; Disdier, A.; Braillon, J.; Stollo, A.; Bourdon, D.; Maccari, A., In air durability study of solar selective coating for parabolic trough technology. *AIP Conf. Proc.* **2017**, *1850*, 130010, 1-8.
57. Bergman, T. L.; Lavine, A. S.; Incropera, F. P.; Dewitt, D. P., *Fundamentals of Heat and Mass Transfer.* 7th ed.; John Wiley & Sons: New Jersey, USA, 2011.

58. Surblys, D.; Matsubara, H.; Kikugawa, G.; Ohara, T., Application of atomic stress to compute heat flux via molecular dynamics for systems with many-body interactions. *Phys. Rev. E* **2019**, *99*, 051301(R), 1-6.
59. Boone, P.; Babaei, H.; Wilmer, C. E., Heat Flux for Many-Body Interactions: Corrections to LAMMPS. *J. Chem. Theory Comput.* **2019**, *15*, 5579–5587.
60. Kondratyuk, N. D., Comparing different force fields by viscosity prediction for branched alkane at 0.1 and 400 MPa. *J. Phys.: Conf. Ser.* **2019**, *1385*, 012048, 1-6.

Table of Contents



Synopsis. Pd-based nanofluids were prepared and they showed appealing optical and thermal properties for improving the efficiency of the concentrated solar power plants.